Analyst

Accepted Manuscript

Volume 1 | Number 1 | Jan 2013 | Pages 1–100

Analyst

www.rsc.org/analyst

ROYAL SOCIETY OF CHEMISTRY

ROYAL SOCIETY OF CHEMISTRY

www.rsc.org/analyst

High resolution mass spectrometry imaging of plant tissues: towards a plant metabolite atlas

Dhaka Ram Bhandari[1], Qing Wang[2], Wolfgang Friedt[2], Bernhard Spengler[1], Sven Gottwald[2]*, Andreas Römpp[1]*

[1]Justus Liebig University Giessen, Institute of Inorganic and Analytical Chemistry, Schubertstrasse 60, building 16, 35392 Giessen, Germany; [2]Justus Liebig University Giessen, Department of Plant Breeding, IFZ, Justus Liebig University Giessen, Heinrich-Buff-Ring 26-32, 35392 Giessen, Germany

*Author for correspondence:

Sven Gottwald

Tel: +49641-9937426
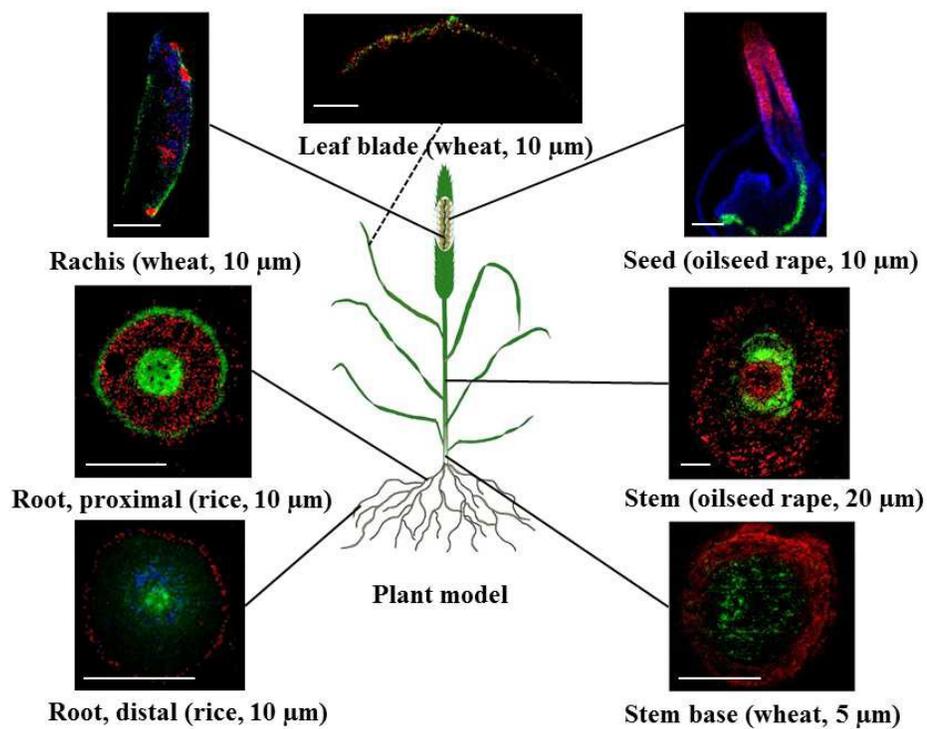
Sven.Gottwald@agrar.uni-giessen.de

Andreas Römpp

Tel: +49641-9934802

Andreas.Roempp@anorg.Chemie.uni-giessen.de

1

Graphical Abstract

Label-free chemical imaging of a wide range of metabolites in all major plant organs acquired at high spatial resolution.

Summary

Mass spectrometry (MS) imaging provides spatial and molecular information for a wide range of compounds. This tool can be used to investigate metabolic changes in plant physiology and environmental interaction. A major challenge in our study was to prepare tissue sections that were compatible with high spatial resolution analysis and therefore dedicated sample preparation protocols were established and optimized for the physicochemical properties of all major plant organs. We combined high spatial resolution (5µm), in order to detect cellular features, and high mass accuracy (< 2 ppm root mean square error), for molecular specificity. Mass spectrometry imaging experiments were perfomed in positive and negative mode. Changes in metabolite patterns during plant development were investigated for germination of oilseed rape. The detailed localization of more than 90 compounds allowed assignments to metabolic processes and indicated possible functions in plant tissues. The 'untargeted' nature of MS imaging allows the detection of marker compounds for the physiological status, as demonstrated for plant-pathogen interaction. Our images show excellent correlation with optical/histological examination. In contrast to previous MS imaging studies of plants, we present a complete workflow that covers multiple species, such as oilseed rape, wheat seed and rice. In addition, different major plant organs and a wide variety of compound classes were analyzed. Thus, our method could be used to develop a plant metabolite atlas as a reference to investigate systemic and local effects of pathogen infection or environmental stress.

Key words: *Fusarium graminearum*, high mass resolution, high spatial resolution, mass spectrometry imaging, metabolites, oilseed rape, wheat

1   Introduction

Plants are major suppliers of food and natural resources used in pharmaceuticals, cosmetics, and fine chemicals. As sessile organisms, plants cannot escape their environment, instead (progressive) acclimatization by specific metabolic adjustments is the only response to changing conditions [1]. This resulted in a complex metabolism with over 200,000 known primary and secondary metabolites [2].

As part of the 'omics' field, metabolic studies have been applied to a wide spectrum of topics in plant science. These include basic research in model plants such as *Arabidopsis* to discover fundamental biosynthetic processes and metabolic networks [3] as well as applied research in crop plants such as wheat (*Triticum aestivum*) and oilseed rape (*Brassica napus*) to uncover biochemical mechanisms behind complex agronomical traits and phenotypes [4]. Important current issues in crop plant research are developmental plasticity [5], responses to abiotic [6] and biotic stress [7]. In contrast to genes, metabolites are the end products of cellular processes and therefore, can serve as direct signatures of biochemical activity [8]. Metabolomics studies are typically based on mass spectrometry (MS), hyphenated with techniques such as gas and liquid chromatography, covering an extensive variety of compound classes and concentration ranges. In these studies, usually homogenized samples are used, resulting in a loss of spatial information. On the other hand, visualization has become an important topic in plant science, because detailed knowledge on metabolite distributions in plants is fundamental for the understanding of local regulatory networks, which underlay selected traits [9]. Visualization is usually achieved by fluorescence microscopy, *in situ* hybridization or immunohistochemistry [10], techniques which provide high spatial resolution, but chemical information is typically limited to very few compounds per experiment.

Mass spectrometry (MS) imaging combines spatial information and molecular information for a wide range of compounds. This method can, therefore, complement the classical approaches of metabolomics studies and microscopic methods. MS imaging is the method of scanning a sample of interest and generating images of the intensity distribution of analyte ions. In contrast to classical histochemical methods, MS imaging is a label free technique and thus, can be used without prior knowledge of the analyte. Due to this untargeted nature, hundreds of compounds can be detected simultaneously. While numerous studies are published in the field of clinical research, plant research is a relatively new application of MS imaging which,

32   however, offers important advantages for the detailed investigation of metabolites from

33   complex plant tissues [7, 11].

34   The first studies using MALDI imaging on plants analyzed the distribution of agrochemical

35   compounds in soya bean (*Glycine max*) [12] and carbohydrates in wheat (*Triticum aestivum*)

36   stem [13]. Subsequent studies included applications on rice (*Oryza sativa*) seeds [14, 15], flowers

37   and roots of the model plant *Arabidopsis thaliana* [16-19] and barley (*Hordeum vulgare*) seeds [20].

38   However, most MS imaging studies in plants were performed with MALDI-TOF instruments,

39   which provide lower mass resolution data, possibly leading to ambiguous results. Only

40   recently, high mass resolution orbital trapping mass analyzers were applied [16, 21-24]. A pixel

41   size of 25 μm [25, 26] and 5μm [27] was obtained in selected experiments, but most studies were

42   performed at 100 to 200 μm spatial resolution. A related method is laser desorption ionization

43   (LDI) which was used for the analysis of plant tissue with a TOF mass spectrometer at 10 μm

44   pixel size.[28] This approach does not require any matrix application, but is limited to

45   compounds with UV-absorbing functional groups.

46   We have introduced a MS imaging method that combines for the first time high selectivity (1

47   ppm mass accuracy) and high spatial resolution (3 to 10 μm pixel size) in one experiment [29].

48   This results in a significantly improved reliability of compound identifications and provides

49   molecular information on a cellular level. This technique was initially developed for

50   mammalian tissues [30], but has now been further developed and optimized for non-mammalian

51   tissues. Recently, we have demonstrated the applicability of MS imaging for metabolite

52   characterizations of wine (*Vitis vinifera*) grapes [31], the bird's nest fungus *Cyathus striatus* [32]

53   and the licorice (*Glycyrrhiza glabra*) rhizome [33] at 20 μm, 15 μm and 10 μm pixel size,

54   respectively.

55   Previous MS imaging studies of plants were limited to a selected organ in a particular species

56   and typically focused on a certain compound class. In this publication we present new

57   developments in MS imaging of plant tissues that enable a comprehensive investigation of the

58   plant metabolome. These developments include the first MS imaging experiments at 5 μm

59   pixel size which reveal the detailed structure of metabolites in plant organs. We were able to

60   image a wide range of compound classes including different phenolic compounds,

61   phospholipids and other lipid species, carbohydrates, phenolic choline esters, glycosides, and

62   glycerides in mature and germinating oilseed rape. These data probably represent the most

63   comprehensive spatially resolved information about metabolites in plants, so far.

64   To establish a plant metabolome atlas, it is necessary to analyze all relevant plant organs and

65   to cover different plant species. This primarily concerns the development of dedicated sample

66 preparation techniques. In plants, different organs and tissues are specialized and modified for

67 specific functions. Thus sample preparation techniques need to be adapted to the different

68 plant organs and (metabolic) stages. Consequently, we also present developments in MS

69 imaging, which concern sectioning procedures that were optimized for high spatial resolution

70 analysis in a variety of tissues with specific physicochemical properties.

71 The methodological approach and obtained information of MS imaging is discussed in detail

72 in a case study comparing mature and germinating seed of oilseed rape (section 2.1).

73 Subsequently additional plant species and organs are discussed. This includes experiments in

74 negative ion mode and with 5 μm pixel size for wheat seed (2.2). Sample preparation is the

75 focus for wheat rachis (2.3), wheat stem base (2.4) and rice root (2.5). Finally, we show an

76 example in which a wheat seed infected by the fungal pathogen *Fusarium graminearum* is

77 compared to an uninfected seed and cultured fungal mycelium (2.6). Details of the

78 experimental procedure for each experiment in particular sample preparation are discussed in

79 Experimental section (3.).

80 In the Conclusions section (4.) we have included measurements of additional plant organs

81 (distal root, leaf and stem). We also discuss the idea of how our MS imaging approach could

82 be used to build up an atlas of the plant metabolome as a reference to detect systemic and

83 local metabolic changes.

84

85

86

2   Results and Discussion

2.1   Mapping of metabolic processes in seed development

Maturity and germination are metabolically highly active stages during the development with significant implications for subsequent plant performance [35, 36] and nutritional quality of seed products [37]. Therefore, these stages were chosen to establish high resolution MS imaging as a tool for mapping metabolites.

Seeds of oilseed rape are 2-3 mm in diameter, which makes direct cryosectioning challenging. Therefore, cellulose (CMC) solution was used as an embedding material as described in the experimental section. The optical image of both the stages (Fig. 1a and 1b) can be directly correlated to the respective ion images (Fig 1c, 1e, 1d 1f). A mass spectrum acquired from a single 10 μm pixel in the shoot apical meristem region of germinating seed is shown in Fig. 1g. The exact location of this pixel and the zoomed-in mass spectrum are provided in Supporting Information, Fig. S1. Additional single 10 μm spectra from cotyledon vasculature, nucellar tissue (putative), seed coat, and emerging radicle are shown in the Supporting Information, Fig. S2-S5. Several compounds such as sinapine, methyl sinapate, cyclic spermidine conjugate, triacylglycerols and phosphatidylcholines were detected. These compounds were identified based on accurate mass measurements. For example, sinapine (choline ester of sinapic acid) was detected with a mass error of -0.83 ppm (Fig. 1g) and the corresponding image is shown in Fig. 1c (blue). The root mean square error (RMSE), calculated from 52523 spectra over the full image, was 1.0 ppm. The mass accuracy was better than 2 ppm for all compounds assigned in this article. This demonstrated a reliable detection of compounds also under imaging conditions. Using high resolution and high mass accuracy, it is possible to generate MS images with a narrow bin width of $\Delta m/z = \pm 5$ ppm, thus preventing interference from neighboring peaks (an example is discussed for the MS imaging on wheat seed). This bin width was used for all MS images presented in this study. A list of 93 compounds imaged in oilseed rape (including mass accuracy values) is given in Supporting Information, Table S1, and the respective MS images are compiled in Supporting Information, Fig. S6 (germination) and Fig. S7 (maturation). The sequential numbering of compounds in Table S1 corresponds to the index numbers in Fig. S6 and Fig. S7. For example, the MS images of sinapine (compound No. 1) are shown in Fig. S6.1 and Fig. S7.1. These images are selected ion images of a single compound (allowing visualization of pixels with lower signal intensities), in contrast to the combined RGB images in Fig. 1.

119 The compound identification can be further assisted by on-tissue MS/MS experiments as

120 demonstrated for sinapine in Fig. 1h, showing the single pixel on-tissue tandem mass

121 spectrum. The fragment ion at *m/z* 251 corresponds to a loss of trimethylamine from the

122 choline group. Additional fragment ions can be attributed to sequential loss of C_2H_4O (*m/z*

123 207), CH_3OH (*m/z* 175) and CO (*m/z* 147). All fragment ions were detected with a mass error

124 of less than 1 ppm. This fragmentation pattern is also in accordance with electrospray-based

125 MS/MS data [38], thus confirming the initial identification which was based on accurate mass

126 data.

127 In the mature seed, sinapine was distributed throughout the entire embryo (Fig. 1d, blue)

128 which consists of the cotyledons and the hypocotyl-radicle region (Fig. 1b). This broad

129 distribution of sinapine was found to persist during the early germination (Figure 1c, blue). In

130 contrast, cyclic spermidine conjugate showed a distinct distribution in the hypocotyl-radicle

131 region in the mature seed (Fig. 1d, red, appears magenta due to overlay with sinapine in blue),

132 and in the germinating seed their activities shifted to the emerging radicle (Fig. 1c, red). This

133 demonstrates that MS imaging is able to detect shifts in metabolite distribution at different

134 developmental stages. Since a second spermidine conjugate, the N1,N5,N10-tricaffeoyl

135 spermidine, showed a similar spatial distribution (Fig. 1e and 1f red), our results suggest that

136 spermidine conjugates play a role in the development of the hypocotyl-radicle, which later

137 differentiates into the plant root and stem (a more detailed discussion is given in Supporting

138 Information, Notes S1).

139 The distribution of the compounds mentioned above corresponds very well to the hitherto

140 only tissue-specific metabolite mapping in oilseed rape, carried out by combining laser

141 microdissection and HPLC-DAD/MS [39]. This demonstrates both the ability of MS imaging to

142 confirm findings from alternative techniques and significantly improve details on spatial

143 distributions. The approach applied by Fang et al. [39] allowed differentiating between inner and

144 outer cotyledon in the mature seed. MS imaging at high spatial resolution, however, enabled

145 to allocate metabolites to more detailed morphological features. For instance, sinapoyl

146 glucose, previously identified in a bulk analysis of oilseed rape [40], was mapped at both seed

147 developmental stages to a thin layer between the two cotyledons (Fig. 1c, d, green). This

148 region corresponds to the adaxial (upper) cotyledon epidermis which also contained different

149 kaempferol derivates (Fig. S6.30-6.33; Fig. S71.30-7.33). Therefore, these compounds might

150 contribute to the epidermal shield against various abiotic stress factors such as UV-B

151 radiation [41, 42]. In contrast, the choline ester 'UC#1' was mapped at both seed stages in the

152 outer layer of cotyledons, representing the abaxial (lower) cotyledon epidermis (Fig. 1e, f,

153 blue). UC#1 belongs to a group of 'unknown' choline esters which were initially detected in

154 mature oilseed rape [43] [44]. The possibility to map compounds even in the epidermis layers,

155 makes MS imaging an interesting tool to examine metabolomic processes.

156 Feruloylcholine guaiacyl (FC(4-O-8')G) was distributed throughout the mature embryo (Fig.

157 1f, green), but demonstrated different and more specific accumulations in the germinating

158 embryo, i.e. in the parenchyma layer of emerging hypocotyl and shoot apical meristem (Fig.

159 1e, green). The general presence of feruloylcholine FC(4-O-8')-guaiacyl in oilseed rape has

160 previously been reported [43].

161 MS imaging is a direct analysis, which does not require preliminary extraction to detect a

162 wide range of compound classes from a single tissue section. In fact, the obtained results were

163 in agreement with other untargeted hyphenated-MS techniques which used extraction of the

164 whole seed [43, 44] or more specific analysis including laser microdissection and HPLC-

165 DAD/MS [39]. The high-resolution images generated by our MS imaging method provide much

166 more detailed spatial distributions, which enable elucidation of biological metabolite

167 functions.

168 This data can be used to investigate metabolomic networks. An example is the sinapate ester

169 metabolism presented in Fig. 2, Fig. S8 and Fig. S9, which is relevant for oil production [46]. In

170 this pathway not only abundant metabolites such as sinapine, coumaric acid and kaempferol

171 compounds were mapped, but also less abundant compounds such as methyl sinapate with

172 unknown functions. So far, methyl sinapate has rarely been reported [43, 47]. MS imaging has

173 located this compound in the entire mature embryo as well as in the outer cotyledon,

174 hypocotyl and radicle in the germinating stage (Fig. 2). Since the biological function of

175 methyl sinapate is still unknown, it was interesting to find them remarkably enriched in the

176 central apical shoot meristem (Fig. 2), indicating a possible function in the developing

177 hypocotyl. More details on sinapine esters and kaempferol glycosides are shown in

178 Supporting Information, Notes S2.

179

180 **2.2   Wheat seed**

181 Wheat seed at the soft dough stage of maturity are physiologically mature, but still

182 characterized by rapid accumulations of starch and nutrients [48]. In contrast to oilseed rape,

183 wheat seed (dough stage) have higher moisture content (about 40%), but are still elastic

184 compared to the later stages, such as the postharvest state, which has been analyzed for

185 oilseed rape. The size and the shape of the wheat seed allowed direct mounting in the

186 cryomicrotome without embedding. This allows tissue section preparation by direct

187 cryosectioning. The optical image (Fig. 3a) from a transverse section of germ-region

188 (embryo) can be directly correlated to MS images (Fig. 3b). In addition to sample preparation,

189 spatial resolution and mass resolution are central parameters for generating high-quality

190 images in untargeted metabolite screening. An important reason is the lack of

191 chromatographic separation, which makes analyte assignments in MS imaging more

192 complicated compared to metabolomic analysis based on GC/MS or LC/MS [16]. We combined

193 high mass resolution (which allows generating images with a narrow *m/z* bin width of ± 5

194 ppm) with high spatial resolution (5 μm pixel size). This enabled to represent the grain

195 architecture with a reliable assignment of imaged metabolites to their respective *in-situ*

196 locations. For example, it was possible to demonstrate the specific location of a polyphenol

197 glycoside in the protection sheath coleoptile/coleorhizae (Fig. 3b, green), suggesting a

198 function in protecting the emerging shoot, plumules and/or radicle against UV-B radiation,

199 pathogens or herbivores [49]. In addition, a phosphatidylcholine PC(36:4) was specifically

200 located in the scutellum (Fig. 3b, blue), while a phosphatidylglycerol PG(38:2) was restricted

201 to the pericarp-seed coat region (Fig. 3b, red). PG membrane lipids are vital for normal

202 embryo development as they are involved to form chloroplast thylakoid membranes, which

203 are the primary site of photosynthesis [50]. By contrast, high mass resolution (± 5 ppm)

204 combined with low spatial resolution results in a loss of spatial information (Fig. 3c), which

205 shows the same measurement with a recalculated pixel size of 50 μm. A critical loss of

206 information is also observed using a bin width of 0.1, as typically used for MALDI-TOF

207 imaging experiments. Here, low mass resolution affects the image generation due to the

208 interference of neighboring peaks (Fig. 3d). Consequently, a combination of high mass

209 resolution with high spatial resolution is needed to resolve the complexity of metabolites in

210 plant tissue sections.

211 Negative ion mode measurements provide a possibility to obtain complementary information

212 on identification of the compounds. A section of the wheat germ similar to Fig. 3a was

213 scanned in negative ion mode (Fig. 4a). For example, the polyphenol glycoside in Fig. 3b

214 (green) was confirmed by having the same spatial distribution in negative ion mode (Fig. 4b,

215 green). Similar distribution of additional polyphenol glycosides is demonstrated by comparing

216 positive and negative ion measurements (Fig. S10). Moreover, the negative mode experiment

217 enables imaging of additional compound classes such as a phosphatidylinositol [PI(34:2)-H]-

218 located in the scutellum and endosperm of wheat seed (Fig. 4b, red). PI is a key membrane

219 constituent and an important participant in signaling processes in seed and vegetative tissue [51, 52], responsible for normal plant growth, stress response and seed germination [53 54].

2.3 Wheat spike rachis

222 The rachis is the primary axis of a cereal spike, which bears the spikelets containing the
223 flowers. The spike rachis consists of low-density tissues, resulting in floating of the specimen
224 in CMC solution (used for oilseed rape, Fig. 1). Therefore, an alternative embedding material,
225 a paste of 15 % (w/v) tragacanth gum in water was employed [55]. The rachis is responsible for
226 the translocation of assimilates into florets and developing seeds [56], but also the passage for
227 systemic inflorescence colonization by fungal pathogens such as *Fusarium graminearum* in
228 wheat [57] or *Aspergillus flavus* in maize [58]. Although recent studies have demonstrated the
229 potential of the rachis as an effective defense structure, the molecular and cellular processes
230 behind these defenses are still unknown [58, 59]. The optical image of a transverse rachis section
231 (Fig. 5a) correlates well with the MS image. The MS image shows a polyphenol glycoside
232 located in the epidermis (Fig. 5b, green) and two further metabolites, a
233 lysophosphatidylcholine (Fig. 5b, blue) and a pheophytin (Fig. 5b, red), spatially distributed
234 in the parenchyma cells, which include the photosynthetically active chlorenchyma. In fact,
235 pheophytin is a chlorophyll derivative involved in the electron transfer pathway of
236 photosystem II [60]. In addition to the above mentioned nutritional aspects, compounds such as
237 lysophosphatidylcholine are essentially involved in plant health by functioning in the
238 synthesis of phyto-oxylipins which comprise, for example, antifungal peptides and defense-
239 signaling molecules [61].

240

2.4 Wheat stem base

242 As the gateway from below- to above-ground plant parts, the stem base is a neuralgic point
243 for the spread of soil-borne pathogens into the upper plant organs [62]. The stem base of wheat
244 seedlings has a relatively high water content compared to seed or rachis. Thus, a faster
245 freezing method was obtained by using a coolant mixture of dry ice and hexane. The diameter
246 of a stem base is relatively small for a low spatial resolution measurement. Therefore, a 5 μm
247 step size was selected for MS imaging. As examples, the optical image (Fig. 6a) is well
248 correlated with the ion image, where a polyphenol glycoside was mapped specifically to the
249 leaf sheath (Fig. 6b, red), while a phospholipid was enriched in the stem tissue (Fig. 6b,
250 green). Similarly to the lysophosphatidylcholine reported from the rachis,
251 phosphatidylcholines are involved in the synthesis of phyto-oxylipins such as jasmonates [61]

252 which are currently discussed as essential signaling molecules in wheat defences against *F.*

253 *graminearum* [63]. Changes in these phospholipids occur at the site of fungal infection, since

254 they are rapidly formed in response to pathogen attacks, which makes them useful markers for

255 induced resistance [64]. Thereby, spatial distributions in diseased tissues could facilitate the

256 identification of resistance-related lipids.

257

2.5 Plant roots

259 Roots remained largely unexplored for quite a long time [65]. The soil micro-flora living

260 directly at the surface or within roots facilitates pathogenic interactions and cooperative

261 interactions. The latter improve nutrient uptake, stress resistance and yield performance [67].

262 Root development and physiology are highly flexible in changing environments. However,

263 the chemical signaling behind these changes, as well as behind the root-microbe interactions

264 is largely unknown [68].

265 With this background, roots represent an important target for an MS imaging application.

266 First studies towards a procedure that meets the specific requirements of roots, have been

267 conducted on *in vitro*-grown roots of wheat, barley and rice. Cereals have a fibrous system of

268 thin seminal roots with a typically high water content and fragile structure, characteristics that

269 challenge the preparation of tissue sections. The CMC embedding and sectioning in a

270 cryomicrotome as described for aerial plant parts was not successful for root tissue. The large

271 vacuole in the root cell caused the cells to rupture due to the change in temperature (during

272 thawing process). Thin and uniform root cross sections were only obtainable with a common

273 shaving blade.

274 Seminal root tissues were found to be generally very fragile, and the structure integrity was

275 easily lost. While rice root sections were on average 0.8 mm in diameter, wheat and barley

276 root sections were not more than 0.5 mm in diameter. In case of rice roots, it was possible to

277 generate cross sections that were appropriate for MS imaging measurements (Fig. 7a), for

278 wheat and barley the limiting factor was a high fragility together with a low diameter, which,

279 so far, hampers the preparation of cross sections with sufficient quality. Consequently, the MS

280 imaging measurements resulted in low quality ion images, which were not suitable for fine-

281 scale metabolite localization. However, we were able to image a cross section from the

282 elongation zone of seminal rice roots, which had a diameter (ca. 500 μm) similar to wheat and

283 barley roots (Fig. S11). This is most likely related to the fact that root cells in this zone are in

284   the state of elongation, and their vacuoles are less filled with water, leading to a more stable

285   tissue structure.

286   The optical image of a rice root shows the main compartments: root hair; epidermis; cortex;

287   endodermis; and stele containing the vascular bundles and metaxylem vessels (Fig. 7a). The

288   example MS imaging measurement demonstrates the fine-scale localization of a penta-hexose

289   carbohydrate in the root cortex (Fig. 7b, red), and of a phosphatidylcholine mapped to the

290   epidermis and the central stele with a specific absence from metaxylem vessels (Fig. 7b,

291   green). The detected hexose is likely part of the carbohydrate reserves in root cortex. The

292   carbon metabolism generally represents an essential sink-source interaction, in which root and

293   shoot growth influence each other mutually. Consequently, the carbohydrates translocation

294   from leaves and their storage in roots are very sensitive to stresses, management practices and

295   root-microbe interactions. Decreased root reserves are known to profoundly affect plant

296   performance [69, 70]. Thus, carbon use and sugar signaling are of high scientific interest and

297   represent a good example for the applicability of a plant metabolome atlas.

298   **2.6   Markers for *Fusarium* infection**

299   In cereal crops, *F. graminearum* (*Fg*) is a major agent of fungal diseases which cause severe

300   yield reductions and quality deterioration, especially due to mycotoxin accumulations in seeds

301   which are toxic to farm animals and humans [71]. Both the healthy and infected wheat seed have

302   low moisture content (< 20%). Infected wheat seed demonstrates the characteristic weight

303   reduction, shriveled and light-brown appearance due to colonization by *Fg* [72] as shown in the

304   photographic (Fig. 8a, d) and microscopic images (Fig. 8b, e). The characteristic low moisture

305   content in healthy wheat seed and additionally the substantial disease-related physical

306   changes represent a specific challenge for the preparation of thin uniform sections from wheat

307   seed.

308   To meet this intrinsic problem, a tape-based method [73] was adapted, which assists the

309   generation of thin complete sections from hard specimens. A specially prepared adhesive

310   tape, functioning at low temperatures, was attached to the cut surface of sample to support the

311   sectioning. The seed surrounded by CMC as a block, which was formed by freezing CMC in a

312   mold using a cooling mixture. For a comparative MS imaging, healthy and diseased seed of

313   the highly Fusarium head blight (FHB) susceptible wheat cultivar Florence-Aurore were used.

314   The overlay ion images of a healthy (Fig. 8c) and an infected wheat bran (Fig. 8f) show

315   uniform distributions of a tetra-hexose metabolite in the endosperm (Fig. 8f, red). However,

316   several compounds were specifically detected in the bran of the infected seed, e.g. 4-

317   (trimethylammonio)but-2-enoate (Fig. 8f, green). This distribution indicates a relation to the

318   pathogen infection since *Fg* preferably colonizes this peripheral tissue in mature seeds [74]. The

319   localization of *Fg* in this particular sample was confirmed by fluorescence microscopy (Fig.

320   S12). The chemical identity of the fungus-related metabolite (4-(trimethylammonio)but-2-

321   enoate) was confirmed by MS/MS analysis (Fig. S13f). MALDI MS spectra of *Fg* hyphae

322   also resulted in the same metabolite signals (Fig. S13e). In addition, a carnitine metabolite

323   was detected in the infected wheat bran (Fig. S13a, b) and in fungal hyphae (Fig. S13e). Both

324   metabolites belong to the carnitine metabolism, which is quite similar in plants and fungi.

325   However, they were identified from hyphae *in planta* (diseased wheat seed) and from hyphae

326   *in vitro* (culture medium). This indicates a fungal origin and thus, both were denoted as

327   pathogenesis-related metabolites.

328   As demonstrated here, MS imaging can be applied to detect candidates for pathogenesis-

329   related metabolites solely by their spatial distribution within infected parts of a tissue. Such

330   "biomarkers" could be applied to visualize unknown sites of host-pathogen interactions. The

331   few available metabolomic studies on interactions between biotic stressors and plants have

332   already demonstrated that those metabolic processes are highly specific for a given tissue,

333   specie and pathosystem. Therefore, it is conceivable that untargeted MS visualization of

334   metabolomic plant-pathogen interactions will lead to new insights into chemical plant defense

335   mechanisms.

336

337 ## 3   Experimental

338 Detailed information on chemicals and origin of plant material can be found in the supporting

339 information, Methods S1, and Methods S2, respectively.

340 ### 3.1   Sample preparation for MALDI imaging

341 We optimized sectioning procedures like embedding in different media, snapshot freezing,

342 use of adhesive tape and manual sectioning to obtain thin uniform sections. For

343 cryosectioning, water (ice) was used as an adhesive to hold the specimen on a sample holder

344 of a cryomicrotome (HM 525 cryostat, Thermo Scientific, Dreieich, Germany). Sections of

345 10-20 μm thickness were cut at -15 to -25 °C. The sections were thaw-mounted on

346 microscope glass slides (75 x 25 x 1 mm), which were stored at -80 °C until analysis. Prior to

347 matrix application, sections were brought to room temperature in a desiccator to avoid

348 condensation of humidity on the sample surface. An Olympus BX-40 (Olympus Europa

349 GmbH, Hamburg, Germany) microscope was used to capture optical images of the sections

350 before and after matrix application. In case of positive ion mode, a solution of 200 μL

351 2,5-dihydroxybenzoic acid (DHB) (30 mg/mL in acetone:water (50:50, v/v), 0.1 %

352 trifluoroacetic acid), was applied. For negative ion mode, a solution of 200 μL 4-nitroaniline

353 (10 mg/mL in acetone:water (50:50, v/v)) was sprayed with a pneumatic sprayer [75]. Specific

354 details on sample preparation for individual specimen are given in section 3.3.

355 ### 3.2   Instrumentation for MALDI imaging

356 Highly resolved mass spectra were generated with a Fourier transform orbital trapping mass

357 spectrometer (Exactive or Q Exactive, Thermo Fisher Scientific GmbH, Bremen, Germany)

358 coupled   to   atmospheric-pressure   scanning-microprobe   matrix   assisted   laser

359 desorption/ionization imaging source (AP-SMALDI10, TransMIT GmbH, Giessen, Germany)

360 [76] [29]. For desorption/ionization of the analyte a nitrogen laser (LTB MNL-106, LTB, Berlin,

361 Germany) with a repetition rate of 60 Hz and wavelength of 337 nm was used. The laser beam

362 was focused perpendicular to the sample to a laser ablation spot size of 5 μm. The samples

363 were scanned with 5 to 25 μm step size and the target voltage was set to 4.3 kV. The mass

364 spectrometer was operated in positive ion/negative ion mode and spectra were scanned in

365 different mass-to-charge (m/z) ranges and mass resolutions (R), with m/z = 100-1500 and

366 R=50,000 to 140,000 respectively. Automatic gain control was disabled and the ion injection

367 time was set to 500 ms. Internal calibration was achieved by using lock masses from matrix

368   clusters. The cycle time for one pixel at 140,000 resolving power was 1.3 s. A detailed

369   description of measurements parameters for each sample is given below.

370

371   **3.3   Experimental details for individual specimen**

372   **Oil seed rapeseed**

373   Seeds are embedded in 4% (w/v) carboxymethyl cellulose (CMC) solution. Initially, seeds

374   were kept in Tissue-Tek$^®$ molds (15 x 15 x 5 mm) and the CMC solution was poured to

375   embed the seeds. To remove air bubbles, the filled mold was initially kept at -20 °C for 20

376   minutes, and thereafter transferred to -80 °C for 50 to 60 minutes, to form a solid block. These

377   blocks were transferred to a cryomicrotome at -20 °C to obtain thin tissue sections of 20 μm

378   thickness of oilseed rape at germination and maturation stage (Fig. 1a and Fig. 1b). MS

379   images for germinating seed were obtained at a pixel size of 10 μm with 225 x 357 pixels

380   (Fig. 1c and e). For the mature seed, MS images were obtained at a pixel size of 25 μm with

381   100 x 120 pixels (Fig. 1d and f). In both experiments, mass spectra were acquired with. The

382   resolution of the mass spectrometer was set to 50,000 @ *m/z* 200 for a mass range of *m/z* 150-

383   1000 in positive ion mode.

384

385   **Wheat seed**

386   In contrast to oilseed rape, wheat seeds were directly mounted without embedding in the

387   cryomicrotome, enabling tissue section preparation by direct cryosectioning at -25 °C to

388   obtain a 20 μm thick tissue section (Fig. 3a). For MS imaging measurements, an area of 1600

389   x 900 μm^2 (320 x 180 pixels) was scanned with a pixel size of 5 μm (Fig. 3b). The mass

390   spectrometer was set to a resolution of 70,000 @ *m/z* 200 for a mass range of *m/z* 400-1000 in

391   positive ion mode. For the negative ion mode measurement, an area of 2250 x 2250 μm^2 (150

392   x 150 pixels) was scanned with a pixel size of 15 μm (Fig. 4b). The mass spectrometer was

393   set to a resolution of 100,000 @ *m/z* 200 for a mass range of *m/z* 200-1000.

394

395   **Wheat spike rachis**

396   The spike rachis was fixed inside the tragacanth paste 15 % (w/v) and subsequently stored at -

397   80 °C for 30 min to obtain a solid block. The cryomicrotome was used to obtain sections of

398   10 μm thickness at -15 °C (Fig. 5a). After application of the matrix, an area of 2400 x 1000

399   μm^2 (240 x 100 pixels) was scanned with a step size of 10 μm (Fig. 5b). The mass

400   spectrometer was set to a resolution of 100,000 @ *m/z* 200 for a mass range of *m/z* 100-1000

401   in positive ion mode.

402

403   **Wheat stem**

404   Prior to sectioning, the stem base was frozen in a 4% (w/v) CMC solution by using a coolant

405   mixer for faster freezing (dry ice and hexane) due to high water content. After snap freezing,

406   the CMC block was transferred to the cryostat for sectioning, and sections of 20 μm thickness

407   were obtained at -20 °C (Fig. 6a), scanning an area of 1150 x 1050 μm^2 (230 x 210 pixels)

408   with a step size of 10 μm (Fig. 6b). The mass spectrometer was set to a resolution of 70,000

409   @ *m/z* 200 for a mass range of *m/z* 250-1000 in positive ion mode.

410

411   **Rice roots**

412   Root cross sections were taken from the maturation zone of seminal roots. A common shaving

413   blade was used to obtain thin sections. Thereby, a root was held in between a halved

414   Styrofoam®, and afterwards the blade was moved from top to bottom tangential to the

415   Styrofoam®. The obtained thin section was placed on a glass slide (Fig. 7a). MS imaging

416   analysis on root sections was performed in an area of 1100 x 1200 μm^2 (110 x 120 pixels)

417   with 10 μm step size (Fig. 7b). The mass spectrometer was set to a resolution of 50,000 @

418   *m/z* 200 for a mass range of *m/z* 100-1200 in positive ion mode.

419

420   ***Fusarium graminearum* infected wheat seed**

421   Wheat seed were embedded in a 4% CMC solution followed by a snap freezing using a

422   coolant mixture (dry ice and hexane). Subsequently, the block was placed in a cryomicrotome

423   sample holder. Tissue sections of 20 μm thickness were obtained at -20 °C. The adhesive tape

424   was kept over the trimmed sample. Then a uniform smooth surface was use to give light

425   pressure so that the adhesive tape stick to the surface of the sample. Then a twister was used

426   to hold the tape while the cryomicrotome blade was slowly moved to obtain the tissue section

427   on the adhesive tape (Fig 8b, e). Then the adhesive tape with the section was fixed on a glass

428   slide, using a double-sided tape. Matrix was applied on the tissue while the sample was

429   attached to the adhesive tape. In case of the healthy wheat seed, an area of 4100 x 3400 μm^2

430   (205 x 170 pixels) was scanned with a step size of 20 μm (Fig. 8c). In case of the infected

431   seed, which is comparatively smaller in dimension, a step size of 15 μm was used (Fig. 8F).

432   In both cases, the mass resolution was set at 100,000 @ *m/z* 200 for a mass range of *m/z* 100-

433   1000 in positive ion mode.

3.4 Data processing and image generation

434

435 Ion images of selected *m/z* values were generated using the in-house developed MIRION

436 software package [77] with a *m/z* bin width of $\Delta m/z = \pm 5$ ppm. The ion images were normalized

437 to the highest intensity for each ion species separately. RGB images of three different *m/z*

438 values were overlaid and demonstrated simultaneously. Other data processing steps like

439 interpolation, smoothing or normalization to the matrix signals were not needed and were not

440 applied during the image generation process. The MS images in supporting information,

441 Fig. S6, were generated by converting the raw files from the Orbitrap instrument to imzML

442 format [78]. Images were then generated with MSiReader version 0.04 [79] in the batch processing

443 option, based on a predefined theoretical *m/z* value list. Mass accuracies for Table 1 and Table

444 S1 were calculated according to [80] using intensity-weighted average values from all spectra of

445 one image.

446 Literature and METLIN search was used to identify compounds. The compounds were

447 identified using high mass accuracy (< 2 ppm). For subsequent biological interpretation,

448 annotated metabolites were assigned to appropriate metabolome categories and pathways by

449 consulting the web applications KEGG Pathway Maps [81], MetaCyc Pathway [82], and LIPID

450 MAPS [83].

451

4 Conclusions

452

453 In this study, we present an approach for MS imaging of plant metabolites that covers

454 multiple mono- and dicot species, major plant organs and a wide variety of compound classes.

455 Results were in excellent agreement with previous knowledge including bulk sample MS

456 studies and in addition provided new information on the detailed spatial distribution of

457 important plant metabolites. In contrast to classical imaging methods, the analytes in MS

458 imaging do not have to be known upfront. All presented MS imaging measurements are based

459 on accurate mass determination (mass accuracy better than 2 ppm) for reliable identification,

460 and were performed at 5 to 25 μm pixel size in order to visualize small spatial features.

461 Previous MS imaging studies of plants were so far limited to a selected organ in a particular

462 species and focused on a certain compound class. In order to cover a wider range of plant

463 organs, we optimized different preparation methods, which were adapted for the

464 physicochemical properties of the varying plant organs and tissues. Figure 9 summarizes the

465 results presented in this manuscript and also includes additional plant tissues (distal root, leaf

466 and stem) which are discussed in the supplementary information (Fig. S11, S14, S15). This

467 demonstrates that MS imaging is now applicable to the entire plant from head to roots. It

468 covers all plant organs with relevance for current and future studies towards a comprehensive

469 understanding of physiological and molecular mechanisms behind complex traits and

470 environmental adaptations. One application is to investigate changes in metabolites during

471 plant development as shown for mature and germinating seed of oilseed rape. The detailed

472 localization of more than 90 compounds allowed assignments to certain metabolic processes

473 and first clues to functions in plant tissues. The wide range of analyzed compounds also

474 enabled to describe metabolic pathways, as demonstrated for example by the hitherto unseen

475 spatio-temporal distributions of 22 phenylpropanoids representing a metabolomic network

476 associated with sinapate esters which is considered a major component of oilseed rape meal

477 quality.

478 The 'untargeted' nature of MS imaging allows the detection of marker compounds for a

479 specific physiological status, for example to investigate or predict the quality of plant-

480 pathogen interactions. For Fusarium head blight, one of the most devastating diseases

481 affecting grain crops, fungus-specific compounds were detected in infected wheat seed and

482 their distribution matched with florescence labeling.

483 These examples demonstrate the wealth of information that can be obtained from high
484 resolution MS imaging of plant metabolites. If this approach is combined with classical LC-
485 MS/MS approaches and applied on a larger scale it could be used to build up an inventory of
486 the plant metabolome. The long-term goal would be to establish a plant metabolome atlas for
487 different species similar to the human proteome atlas [84] or the *Drosophila melanogaster*
488 metabolome atlas [85]. Similar to the insect field, the first step would be to establish a
489 metabolome atlas for selected species, e.g. wheat as an important crop plant and *Arabidopsis*
490 *thaliana* as a frequently used plant model. The initial generation of a baseline tissue map as
491 initiated with the presented study would be an important step in this direction. Metabolites are
492 the end products of cellular processes and therefore, can provide comprehensive information
493 on a plant's physiological status. Therefore an atlas of biochemical networks can lead to novel
494 insights into metabolic capacities of cells [86], or can be used as reference for profiling studies.
495 For example, in pathogen-interaction studies MS imaging data from infected plants (as shown
496 in section 2.6) could be compared with the atlas data to identify compounds which are
497 specific for this plant physiological status. In general this kind of information can be used as a
498 reference to investigate systemic and local effects of stress (biotic or abiotic), developmental
499 stages as well as wildtype/genotype studies. In addition, the distribution of these markers
500 could give a first indication about their functional role.

501 Therefore the authors are convinced that high resolution MS imaging will provide new
502 valuable insights in many areas of plant research in the future.

503

504 **Acknowledgements**

511

Analyst Accepted Manuscript

512 ## References

513 1. R. M. Pérez-Clemente, V. Vives, S. I. Zandalinas, M. F. López-Climent, V. Muñoz and A.
514   Gómez-Cadenas, *BioMed research international*, 2013, **2013**, 654120.
515 2. R. A. Dixon and D. Strack, *Phytochemistry*, 2003, **62**, 815-816.
516 3. R. Nakabayashi and K. Saito, *Analytical and bioanalytical chemistry*, 2013, **405**, 5005-5011.
517 4. N. Carreno-Quintero, H. J. Bouwmeester and J. J. Keurentjes, *Trends Genet*, 2013, **29**, 41-50.
518 5. C. Brunetti, R. M. George, M. Tattini, K. Field and M. P. Davey, *Journal of experimental*
519   *botany*, 2013, **64**, 4011-4020.
520 6. T. Obata and A. R. Fernie, *Cellular and molecular life sciences : CMLS*, 2012, **69**, 3225-3243.
521 7. D. Balmer, V. Flors, G. Glauser and B. Mauch-Mani, *Frontiers in plant science*, 2013, **4**, 82.
522 8. G. J. Patti, O. Yanes and G. Siuzdak, *Nature Reviews Molecular Cell Biology*, 2012, **13**, 263-
523   269.
524 9. T. Neuberger, H. Rolletschek, A. Webb and L. Borisjuk, in *Lipidomics*, ed. D. Armstrong,
525   Humana Press, 2009, vol. 579, ch. 24, pp. 485-496.
526 10. S. L. Shaw and D. W. Ehrhardt, *Annual Review of Plant Biology*, 2013, **64**, 351-375.
527 11. Y. J. Lee, D. C. Perdian, Z. Song, E. S. Yeung and B. J. Nikolau, *The Plant Journal*, 2012, **70**,
528   81-95.
529 12. A. K. Mullen, M. R. Clench, S. Crosland and K. R. Sharples, *Rapid Communications in Mass*
530   *Spectrometry*, 2005, **19**, 2507-2516.
531 13. S. Robinson, K. Warburton, M. Seymour, M. Clench and J. Thomas-Oates, *New Phytologist*,
532   2007, **173**, 438-444.
533 14. Y. Yoshimura, N. Zaima, T. Moriyama and Y. Kawamura, *PLoS ONE*, 2012, **7**, e31285.
534 15. N. Zaima, N. Goto-inoue, T. Hayasaka and M. Setou, 2010, 2723-2729.
535 16. J. H. Jun, Z. Song, Z. Liu, B. J. Nikolau, E. S. Yeung and Y. J. Lee, *Analytical Chemistry*,
536   2010, **82**, 3255-3265.
537 17. R. Shroff, F. Vergara, A. Muck, A. Svatos and J. Gershenzon, *Proceedings of the National*
538   *Academy of Sciences*, 2008, **105**, 6196-6201.
539 18. V. Vrkoslav, A. Muck, J. Cvačka and A. Svatoš, *Journal of the American Society for Mass*
540   *Spectrometry*, 2010, **21**, 220-231.
541 19. J. Sarsby, M. W. Towers, C. Stain, R. Cramer and O. A. Koroleva, *Phytochemistry*, 2012, **77**,
542   110-118.
543 20. M. Peukert, A. Matros, G. Lattanzio, S. Kaspar, J. Abadía and H.-P. Mock, *New Phytologist*,
544   2012, **193**, 806-815.
545 21. P. Franceschi, Y. Dong, K. Strupat, U. Vrhovsek and F. Mattivi, *Journal of Experimental*
546   *Botany*, 2012, **63**, 1123-1133.
547 22. P. J. Horn, A. R. Korte, P. B. Neogi, E. Love, J. Fuchs, K. Strupat, L. Borisjuk, V. Shulaev, Y.
548   J. Lee and K. D. Chapman, *The Plant Cell Online*, 2012, **24**, 622-636.
549 23. A. R. Korte, Z. Song, B. J. Nikolau and Y. J. Lee, *Analytical Methods*, 2012, **4**, 474.
550 24. R. J. R. Jaeger, M. Lamshöft, S. Gottfried, M. Spiteller and P. Spiteller, *Journal of Natural*
551   *Products*, 2013, **76**, 127-134.
552 25. N. Goto-Inoue, M. Setou and N. Zaima, *Analytical Sciences*, 2010, **26**, 821-825.
553 26. P. J. Horn, J. E. Silva, D. Anderson, J. Fuchs, L. Borisjuk, T. J. Nazarenus, V. Shulaev, E. B.
554   Cahoon and K. D. Chapman, *The Plant journal : for cell and molecular biology*, 2013, **76**, 138-
555   150.
556 27. A. Korte, M. Yandeau-Nelson, B. Nikolau and Y. Lee, *Anal Bioanal Chem*, 2015, **407**, 2301-
557   2309.
558 28. D. Holscher, R. Shroff, K. Knop, M. Gottschaldt, A. Crecelius, B. Schneider, D. G. Heckel, U.
559   S. Schubert and A. Svatos, *Plant J.*, 2009, **60**, 907-918.
560 29. A. Römpp, S. Guenther, Y. Schober, O. Schulz, Z. Takats, W. Kummer and B. Spengler,
561   *Angew. Chem.-Int. Edit.*, 2010, **49**, 3834-3838.
562 30. A. Römpp and B. Spengler, *Histochemistry and Cell Biology*, 2013, **139**, 759-783.
563 31. A. Berisha, S. Dold, S. Guenther, N. Desbenoit, Z. Takats, B. Spengler and A. Römpp, *Rapid*
564   *Commun. Mass Spectrom.*, 2014, **28**, 1779-1791.
565 32. D. Bhandari, T. Shen, A. Römpp, H. Zorn and B. Spengler, *Analytical and Bioanalytical*
566   *Chemistry*, 2014, **406**, 695-704.
567 33. B. Li, D. R. Bhandari, C. Janfelt, A. Römpp and B. Spengler, *The Plant Journal*, 2014, **80**, 161-
568   171.
569 34. K. Wolfram, J. Schmidt, V. Wray, C. Milkowski, W. Schliemann and D. Strack, *Phytochemistry*,
570   2010, **71**, 1076-1084.

Analyst Accepted Manuscript

35. M. J. Holdsworth, W. E. Finch-Savage, P. Grappin and D. Job, *Trends in plant science*, 2008, **13**, 7-13.
36. R. Angelovici, G. Galili, A. R. Fernie and A. Fait, *Trends in plant science*, 2010, **15**, 211-218.
37. P. Koehler, G. Hartmann, H. Wieser and M. Rychlik, *Journal of Agricultural and Food Chemistry*, 2007, **55**, 4678-4683.
38. U. Thiyam, P. Claudia, U. Jan and B. Alfred, *European Food Research and Technology*, 2009, **229**, 825-831.
39. J. Fang, M. Reichelt, W. Hidalgo, S. Agnolet and B. Schneider, *PLoS one*, 2012, **7**, e48006.
40. A. Baumert, C. Milkowski, J. Schmidt, M. Nimtz, V. Wray and D. Strack, *Phytochemistry*, 2005, **66**, 1334-1345.
41. D. Meissner, A. Albert, C. Böttcher, D. Strack and C. Milkowski, *Planta*, 2008, **228**, 663-674.
42. P. Burchard, W. Bilger and G. Weissenböck, *Plant, Cell & Environment*, 2000, **23**, 1373-1380.
43. K. Clauss, E. von Roepenack-Lahaye, C. Bottcher, M. R. Roth, R. Welti, A. Erban, J. Kopka, D. Scheel, C. Milkowski and D. Strack, *Plant Physiology*, 2011, **155**, 1127-1145.
44. J. Mittasch, C. Böttcher, A. Frolov, D. Strack and C. Milkowski, *Plant physiology*, 2013, **161**, 1656-1669.
45. L. Borisjuk, T. Neuberger, J. Schwender, N. Heinzel, S. Sunderhaus, J. Fuchs, J. O. Hay, H. Tschiersch, H.-P. Braun, P. Denolf, B. Lambert, P. M. Jakob and H. Rolletschek, *The Plant cell*, 2013, **25**, 1625-1640.
46. A. Hüsken, A. Baumert, D. Strack, H. C. Becker, C. Möllers and C. Milkowski, *Molecular Breeding*, 2005, **16**, 127-138.
47. M. Noda and M. Matsumoto, *Biochimica et Biophysica Acta (BBA) - Lipids and Lipid Metabolism*, 1971, **231**, 131-133.
48. B. Manning, K. Schulze and T. McNee, in *Wheat growth & development* eds. J. White and J. Edwards, NSW Department of Primary Industries 2007, pp. 71-86.
49. J. B. Harborne and C. A. Williams, *Phytochemistry*, 2000, **55**, 481-504.
50. R. Tanoue, M. Kobayashi, K. Katayama, N. Nagata and H. Wada, *FEBS Letters*, 2014, **588**, 1680-1685.
51. X. Wang, *Current opinion in plant biology*, 2004, **7**, 329-336.
52. H. Xue, X. Chen and G. Li, *Current opinion in plant biology*, 2007, **10**, 483-489.
53. J. A. Engelman, J. Luo and L. C. Cantley, *Nature reviews. Genetics*, 2006, **7**, 606-619.
54. J. Liu, J. Zhou and D. Xing, *PLoS one*, 2012, **7**, e33817.
55. F. Brignole-Baudouin, N. Desbenoit, G. Hamm, H. Liang, J.-P. Both, A. Brunelle, I. Fournier, V. Guerineau, R. Legouffe, J. Stauber, D. Touboul, M. Wisztorski, M. Salzet, O. Laprevote and C. Baudouin, *Plos One*, 2012, **7**, e50180.
56. R. Metzner, M. R. Thorpe, U. Breuer, P. Blumler, U. Schurr, H. U. Schneider and W. H. Schroeder, *Plant Cell Environ*, 2010, **33**, 1393-1407.
57. N. A. Brown, C. Bass, T. K. Baldwin, H. Chen, F. Massot, P. W. Carion, M. Urban, A. M. van de Meene and K. E. Hammond-Kosack, *J Pathog*, 2011, **2011**, 626345.
58. Z. Magbanua, W. Williams and D. Luthe, 2013.
59. N. A. Brown, M. Urban, A. M. van de Meene and K. E. Hammond-Kosack, *Fungal Biol*, 2010, **114**, 555-571.
60. Y. Saga and H. Tamiaki, *Chemistry & Biodiversity*, 2012, **9**, 1659-1683.
61. L. C. van Loon, M. Rep and C. M. J. Pieterse, *Annual Review of Phytopathology*, 2006, **44**, 135-162.
62. A. M. Mudge, R. Dill-Macky, Y. Dong, D. M. Gardiner, R. G. White and J. M. Manners, *Physiological and Molecular Plant Pathology*, 2006, **69**, 73-85.
63. S. Gottwald, B. Samans, S. Lück and W. Friedt, *BMC Genomics*, 2012, **13**, 1-22.
64. C. Tayeh, B. Randoux, F. Laruelle, N. Bourdon, D. Renard-Merlier and P. Reignault, *Lipids as Markers of Induced Resistance in Wheat: A Biochemical and Molecular Approach*, 2013.
65. J. Raaijmakers, T. Paulitz, C. Steinberg, C. Alabouvette and Y. Moënne-Loccoz, *Plant Soil*, 2009, **321**, 341-361.
66. S. E. Smith and F. A. Smith, *Mycologia*, 2012, **104**, 1-13.
67. J. S. Singh, V. C. Pandey and D. P. Singh, *Agriculture, Ecosystems & Environment*, 2011, **140**, 339-353.
68. J. Shen, C. Li, G. Mi, L. Li, L. Yuan, R. Jiang and F. Zhang, *J Exp Bot*, 2013, **64**, 1181-1192.
69. Y. L. Ruan, *Annual review of plant biology*, 2014, **65**, 33-67.
70. L. V. Kravchenko, A. I. Shapozhnikov, N. M. Makarova, T. S. Azarova, K. A. L'vova, I. I. Kostyuk, O. A. Lyapunova and I. A. Tikhonovich, *Russ J Plant Physiol*, 2011, **58**, 936-940.
71. K. Kazan, D. M. Gardiner and J. M. Manners, *Mol Plant Pathol*, 2012, **13**, 399-413.
72. S. Walter, P. Nicholson and F. M. Doohan, *New Phytol*, 2010, **185**, 54-66.

632   73.   T. Kawamoto, *Archives of Histology and Cytology*, 2003, **66**, 123-143.
633   74.   E. M. Del Ponte, J. M. C. Fernandes and G. C. Bergstrom, *Journal of Phytopathology*, 2007,
634   **155**, 577-581.
635   75.   W. Bouschen, O. Schulz, D. Eikel and B. Spengler, *Rapid Commun Mass Sp*, 2010, **24**, 355-
636   364.
637   76.   M. Koestler, D. Kirsch, A. Hester, A. Leisner, S. Guenther and B. Spengler, *Rapid Commun.*
638   *Mass Spectrom.*, 2008, **22**, 3275-3285.
639   77.   C. Paschke, A. Leisner, A. Hester, K. Maass, S. Guenther, W. Bouschen and B. Spengler, *J*
640   *Am Soc Mass Spectrom*, 2013, **24**, 1296-1306.
641   78.   T. Schramm, A. Hester, I. Klinkert, J.-P. Both, R. M. A. Heeren, A. Brunelle, O. Laprévote, N.
642   Desbenoit, M.-F. Robbe, M. Stoeckli, B. Spengler and A. Römpp, *J. Proteomics*, 2012, **75**,
643   5106-5110.
644   79.   G. Robichaud, K. P. Garrard, J. A. Barry and D. C. Muddiman, *Journal of the American*
645   *Society for Mass Spectrometry*, 2013, **24**, 718-721.
646   80.   A. G. Brenton and A. R. Godfrey, *J. Am. Soc. Mass Spectrom.*, 2010, **21**, 1821-1835.
647   81.   M. Kanehisa, S. Goto, S. Kawashima, Y. Okuno and M. Hattori, *Nucleic Acids Research*,
648   2004, **32**, D277-D280.
649   82.   R. Caspi, T. Altman, K. Dreher, C. A. Fulcher, P. Subhraveti, I. M. Keseler, A. Kothari, M.
650   Krummenacker, M. Latendresse, L. A. Mueller, Q. Ong, S. Paley, A. Pujar, A. G. Shearer, M.
651   Travers, D. Weerasinghe, P. Zhang and P. D. Karp, *Nucleic Acids Research*, 2012, **40**, D742-
652   753.
653   83.   E. Fahy, M. Sud, D. Cotter and S. Subramaniam, *Nucleic Acids Research*, 2007, **35**, W606-
654   612.
655   84.   M. Uhlen, P. Oksvold, L. Fagerberg, E. Lundberg, K. Jonasson, M. Forsberg, M. Zwahlen, C.
656   Kampf, K. Wester, S. Hober, H. Wernerus, L. Bjorling and F. Ponten, *Nat Biotech*, 2010, **28**,
657   1248-1250.
658   85.   V. R. Chintapalli, M. Al Bratty, D. Korzekwa, D. G. Watson and J. A. Dow, *PLoS One*, 2013, **8**,
659   e78066.
660   86.   M. Arita, *Proc Natl Acad Sci U S A*, 2004, **101**, 1543-1547.
661
662

Analyst Accepted Manuscript

663   **Fig. 1** Comparative Mass spectrometry imaging of oilseed rape at maturation and early

664   germination stage. Optical images of seeds at (**a**) the early germination and (**b**) the maturation

665   stage: root tip (RT) containing the root apical meristem (RAM); epidermis tissue (Ep),

666   parenchyma tissue (Pa); vascular tissue (Va); shoot apical meristem (SAM); seed coat (S);

667   endosperm (E); putative nucellar tissue (NT); outer and inner cotyledon (OC and IC); abEp

668   (abaxial cotyledon epidermis); adEp (adaxial cotyledon epidermis); hypocotyl (H); radicle

669   (R); hypocotyl-radicle region (HR); and the seed coat-endosperm region (SE). Scale bar, 500

670   μm. Overlay of *m/z* images from early germinating (**c**) and mature (**d**) seeds showing the

671   tissue- and stage-specific spatial distributions of the cyclic spermidine conjugate $[M+H]^+$, *m/z*

672   496.24421 (red); the sinapoly glucose $[M+H-H_2O]^+$, *m/z* 369.11801 (green); and sinapine

673   $[M+H]^+$, *m/z* 310.16490 (blue). Overlay of ion images from early germinating (**e**) and mature

674   (**f**) seeds showing the tissue- and stage-specific spatial distributions of the tricaffeoyl

675   spermidine $[M+K]^+$, *m/z* 534.20009 (red); feruloylcholine FC(4-O-8')G $[M+H]^+$, *m/z*

676   476.22789 (green); and the phenolic choline ester UC#1 $[M+H]^+$, *m/z* 328.24824 (blue). (**g**)

677   Single pixel MS spectrum obtained at 10 μm pixel size measurement in the early germinating

678   seed. Different classes of compounds, such as sinapine, carbohydrate and lipids were

679   identified based on high mass accuracy. (**h**) On tissue MS/MS of sinapine from a 10 μm pixel.

680   R = mass resolution.

681

682 **Fig. 2** Scheme of metabolomic network associated with sinapate ester metabolism, localized

683 by high-resolution MS imaging in mature and early germinating oilseed rape. Spatial

684 distributions are shown in the ion images below the respective metabolites (left image: mature

685 seed; right image early germinating seed). Blue boxes marked by a white cross indicate that

686 the metabolite has not been detected at that developmental seed stage. Localized key

687 metabolites are marked in bold letters. The sinapate ester metabolism is highlighted as a grey

688 box. The shikimate pathway as gateway to the displayed branch of phenylpropanoid

689 metabolism is indicated as light blue box. The scheme was redrawn based on Clauss et al. [43].

690 Abbreviations: G, guaiacyl moiety; Glc, glucoside; Hex, unknown hexose moieties

691 (commonly Glc); S, syringyl moiety; Soph, sophorose.

692

693 **Fig. 3** Mass spectrometry imaging of a wheat seed section at the soft dough stage with

694 different mass and spatial resolutions. (**a**) Optical image of a 20 μm cross section taken from

695 the germ. The image shows the coleoptile/coleorhiza (Co), the scutellum (Sc), and the

696 pericarp-seed coat region (PS). Scale bar, 500 μm. (**b**) Overlay of three ion images generated

697 with high mass resolution (± 5 ppm) and high spatial resolution (5 μm). The overlay shows

698 the tissue-specific spatial distributions of a polyphenol glycoside $[M+K]^+$, *m/z* 603.11107

699 (green) in the protection sheath coleoptile/coleorhiza covering the main compartments shoot,

700 plumules (first true leaves) and radicle; a phosphatidylcholine $[PC(36:4)+K]^+$, *m/z* 820.52531

701 (blue) in the scutellum (monocot cotyledon); and a phosphatidylglycerol $[PG(38:2)-H_2O+H]^+$,

702 *m/z* 785.56910 (red) in the pericarp-seed coat region. MS images were acquired in positive

703 ion mode with 320 x 180 pixels; 5 μm pixel size; and *m/z* bin width: $\Delta m/z = \pm 5$ ppm. (**c**)

704 Overlay of three ion images generated with high mass resolution (± 5ppm) and low spatial

705 resolution (50 μm pixel size) resulting in a loss of spatial information. (**d**) Overlay of three

706 ion images generated with low mass resolution ($\Delta m/z = 0.1$ bin width) and high spatial

707 resolution (5 μm) resulting in a much less distinct resolution, due to neighboring peaks of

708 similar masses which interfere the image generation.

709

710 **Fig. 4** Mass spectrometry imaging in negative ion mode of wheat seed at soft dough stage. (**a**)

711 The optical image of the 20 μm seed cross section shows the coleoptile/coleorhiza (Co),

712 scutellum (Sc), the endosperm (E), the pericarp-seed coat region (PS), and crease (Cr). Scale

713 bar 500 μm. (**b**) Overlay of ion images shows the tissue-specific spatial distributions of a

714 polyphenol glycoside $[M-H]^-$, *m/z* 563.14063 (green) detected in the embryonic protection

715   sheath coleoptile/coleorhiza covering the main compartments shoot, plumules (first true

716   leaves) and radicle; and a phosphatidylinositol [PI(34:2)-H]⁻, *m/z* 833.51855 (red) located in

717   the scutellum and endosperm, but absent from the crease. MS images were generated with

718   150 x 150 pixels; 15 μm pixel size; *m/z* bin width: $\Delta m/z = \pm 5$ ppm.

719

720   *Fig. 5* Mass spectrometry imaging of a wheat rachis section at soft dough stage. (**a**) Optical

721   image of a 10 μm rachis cross section taken under UV-light. The section was obtained from

722   the center section of inflorescence and shows the epidermis (Ep) and the vascular bundles

723   (Vb) as round inclusions within the central parenchyma cells (Pa). Scale bar 500 μm. (**b**)

724   Overlay of ion images showing the tissue-specific distributions of a polyphenol glycoside

725   [M+H]⁺, *m/z* 565.15518 (green) in the epidermis; a lysophosphatidylcholine

726   [lysoPC(16:0)+K]⁺, *m/z* 534.29565 (blue) in the parenchyma; and a pheophytin [pheophytin

727   a+K]⁺, *m/z* 909.52908 (red) observed in the parenchyma and epidermis. MS images were

728   generated with 240 x 100 pixels; 10 μm pixel size; *m/z* bin width: $\Delta m/z = \pm 5$ ppm.

729

730   **Fig. 6** MS imaging of a wheat crown at seedling stage. (a) The optical image of a 20 μm

731   crown cross section shows the attached leaf sheath (LS) and the anatomy of seedling stem

732   comprising the epidermis (Ep); the cortex (Co); and the pith (Ph) as central portion including

733   the vascular bundles (Vb). Scale bar 500 μm. (b) Overlay of ion images showing the spatial

734   distributions of a polyphenol glycoside [M+K]⁺, *m/z* 565.15518 (red) the leaf sheath; and a

735   phosphatidylcholine [PC(36:4)+K]⁺, *m/z* 820.52531 (green) enriched in the vascular tissues

736   and evenly spread within the cortex. MS images were generated with 230 x 210 pixels; 5 μm

737   pixel size; *m/z* bin width: $\Delta m/z = \pm 5$ ppm.

738

739   **Fig. 7** Mass spectrometry imaging of a seminal rice root. (**a**) Optical image of a cross section

740   of a seminal root taken from a region proximal to stem (maturation zone). The image shows

741   the root hairs (Rh) attached to the epidermis (Ep); the central cortex (Co); the endodermis

742   (En) which separates a central root column (stele) containing the vascular bundles (Vb) and

743   the metaxylem vessels (Mx). The holes visible in the cortex are artefacts caused by the drying

744   of root section in the desiccator. Scale bar 500 μm. (**b**) Overlay of ion images showing the

745   spatial distributions of a [Penta-hexose+K]⁺, *m/z* 867.23784 (red) in the cortical layer, and a

746   phosphatidylcholine[PC(36:4)+K]⁺, *m/z* 820.52531 (green) in the epidermis and the entire

747   stele, except the metaxylem vessels. MS images were generated with 110 x 120 pixels; 10 μm

748   pixel size; *m/z* bin width: Δ*m/z* = ± 5ppm.

749

750   **Fig. 8** Comparative Mass spectrometry imaging of uninfected and *F. graminearum*-infected

751   wheat seeds at ripening stage. The photographic images show a healthy seed (**a**) and a seed

752   infected by the fungal pathogen *F. graminearum* (**d**) a causal agent of the head blight disease.

753   The seeds were sampled from the highly FHB susceptible spring wheat cv. Florence-Aurore.

754   Scale bars 500 μm. The optical images show 20 μm transverse sections of a healthy (**b**) and

755   infected seed (**e**), which were prepared by using the Kuwamoto method. Scale bars 500 μm.

756   Both the photographic (**d**) and the optical image (**e**) of the infected seed demonstrate the

757   characteristic weight reduction, shriveled and light-brown appearance associated with a highly

758   susceptible reaction to the FHB disease. The overlay of ion images of healthy (**c**) and infected

759   seed (**f**) show the spatial distribution of a [tetra-hexose+K]$^+$ metabolite, *m/z* 705.18502 (red)

760   in the entire endosperm. In contrast, the metabolite 4-(trimethylammonio)but-2-enoate

761   [M+K]$^+$, *m/z* 182.05779 (green) located in the entire seed bran and germ was only detected in

762   *F. graminearum* infected seeds. MS images of healthy seed were generated with 205 x 170

763   pixels; 20 μm pixel size; *m/z* bin width: Δ*m/z* = ± 5ppm. MS images of infected seed were

764   generated with 155 x 105 pixels; 15 μm pixel size; *m/z* bin width: Δ*m/z* = ± 5 ppm.

765

766   **Fig. 9** Overview on the different plant structures which have been made available to high-

767   resolution MS imaging. Scale bars in all images 500 μm. (a) Sketch of a plant. (b) MS image

768   of wheat inflorescence rachis measured at 10 μm pixel size, details are given in Fig. 5. (c) MS

769   image of a seminal proximal rice root (maturation zone) measured at 10 μm pixel size; details

770   are given in Fig. 7. (d) MS image of a seminal distal rice root (elongation zone) measured at

771   10 μm pixel size, details are given in Supporting information, Fig. S11. (e) MS image of a

772   wheat leaf blade measured at 10 μm pixel size, details are given in Supporting information,

773   Fig. S14. (f) MS image of germinating oilseed rape at 10 μm pixel size, details are given in

774   Fig. 1. (g) MS image of oilseed rape stem at 20 μm pixel size, details are given in Supporting

775   information, Fig. S15. (h) MS image of wheat stem base at 5 μm pixel size, detail are given in
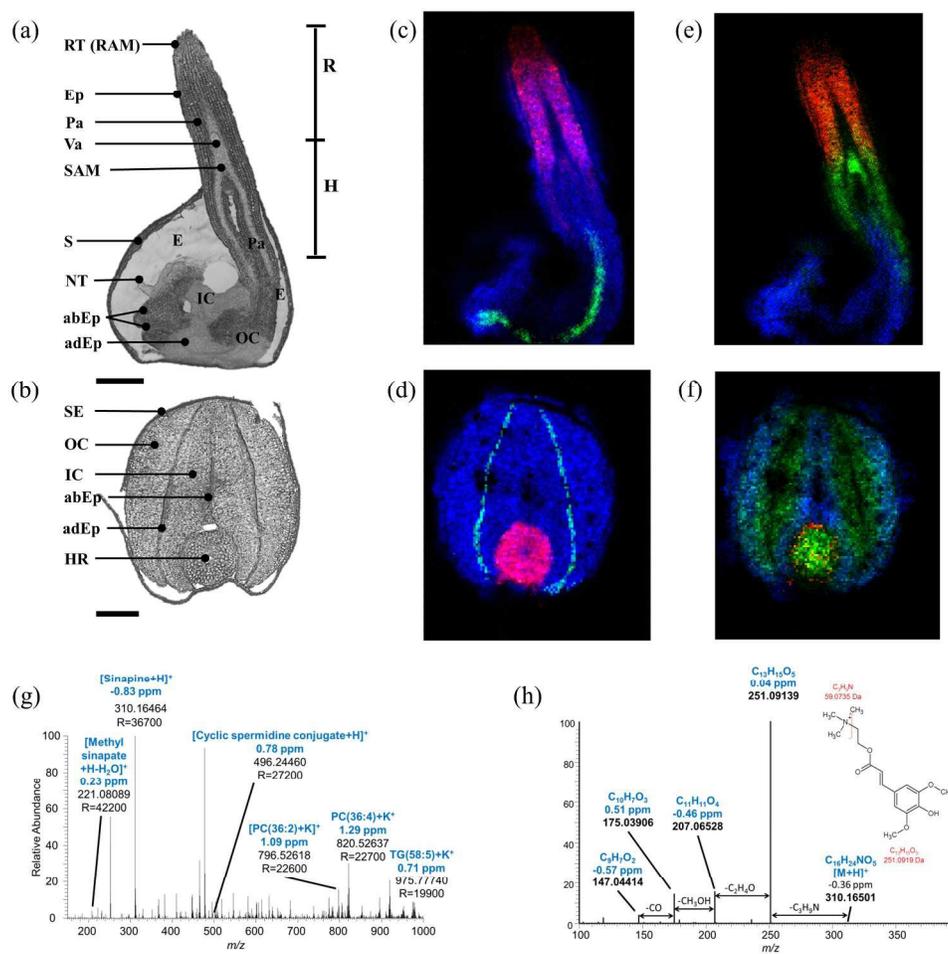
776   Fig. 6.

Fig. 1 Comparative Mass spectrometry imaging of oilseed rape at maturation and early germination stage. Optical images of seeds at (a) the early germination and (b) the maturation stage: root tip (RT) containing the root apical meristem (RAM); epidermis tissue (Ep), parenchyma tissue (Pa); vascular tissue (Va); shoot apical meristem (SAM); seed coat (S); endosperm (E); putative nucellar tissue (NT); outer and inner cotyledon (OC and IC); abEp (abaxial cotyledon epidermis); adEp (adaxial cotyledon epidermis); hypocotyl (H); radicle (R); hypocotyl-radicle region (HR); and the seed coat-endosperm region (SE). Scale bar, 500 µm. Overlay of m/z images from early germinating (c) and mature (d) seeds showing the tissue- and stage-specific spatial distributions of the cyclic spermidine conjugate [M+H]+, m/z 496.24421 (red); the sinapoly glucose [M+H-H2O]+, m/z 369.11801 (green); and sinapine [M+H] +, m/z 310.16490 (blue). Overlay of ion images from early germinating (e) and mature (f) seeds showing the tissue- and stage-specific spatial distributions of the tricaffeoyl spermidine [M+K]+, m/z 534.20009 (red); feruloylcholine FC(4-O-8')G [M+H]+, m/z 476.22789 (green); and the phenolic choline ester UC#1 [M+H]+, m/z 328.24824 (blue). (g) Single pixel MS spectrum obtained at 10 µm pixel size measurement in the early germinating seed. Different classes of compounds, such as sinapine, carbohydrate and lipids were identified based on high mass accuracy. (h) On tissue MS/MS of sinapine from a 10 µm pixel. R = mass resolution.
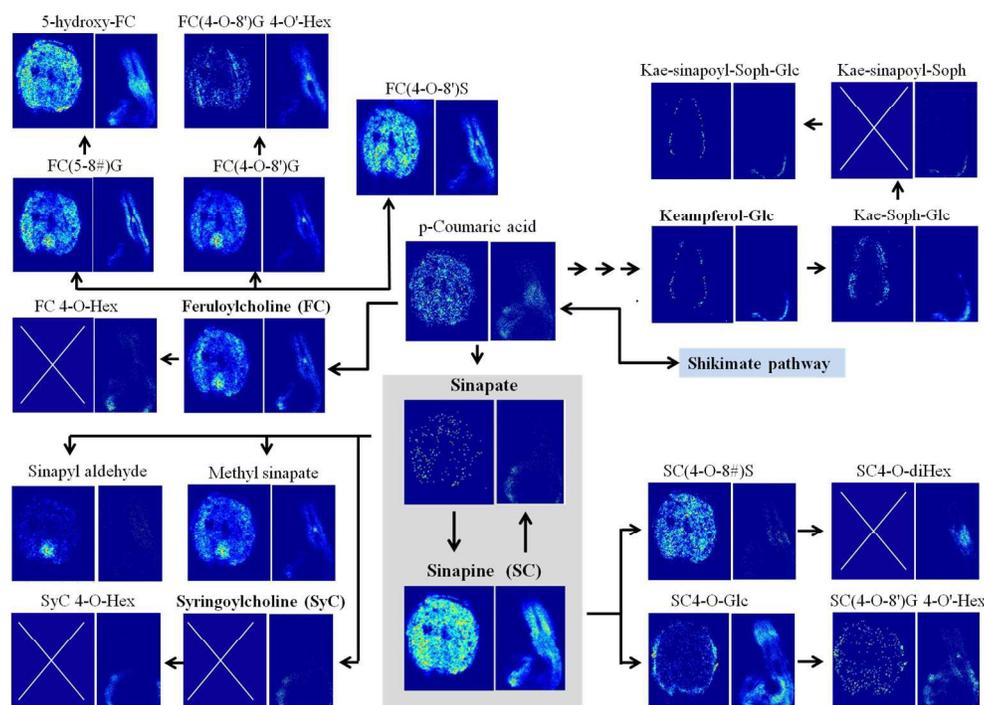255x251mm (260 x 260 DPI)

Fig. 2 Scheme of metabolomic network associated with sinapate ester metabolism, localized by high-resolution MS imaging in mature and early germinating oilseed rape. Spatial distributions are shown in the ion images below the respective metabolites (left image: mature seed; right image early germinating seed). Blue boxes marked by a white cross indicate that the metabolite has not been detected at that developmental seed stage. Localized key metabolites are marked in bold letters. The sinapate ester metabolism is highlighted as a grey box. The shikimate pathway as gateway to the displayed branch of phenylpropanoid metabolism is indicated as light blue box. The scheme was redrawn based on Clauss et al. 43. Abbreviations: G, guaiacyl moiety; Glc, glucoside; Hex, unknown hexose moieties (commonly Glc); S, syringyl moiety; Soph, sophorose.
254x190mm (300 x 300 DPI)
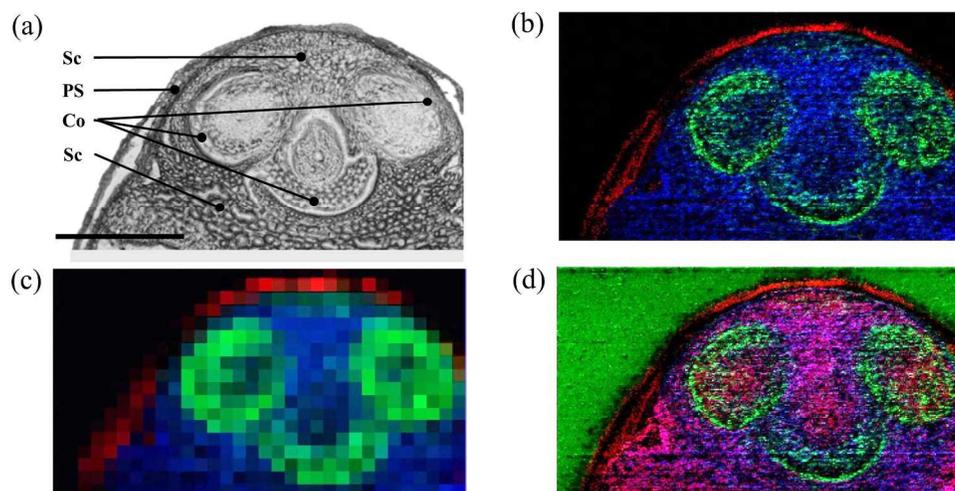
Fig. 3 Mass spectrometry imaging of a wheat seed section at the soft dough stage with different mass and spatial resolutions. (a) Optical image of a 20 µm cross section taken from the germ. The image shows the coleoptile/coleorhiza (Co), the scutellum (Sc), and the pericarp-seed coat region (PS). Scale bar, 500 µm. (b) Overlay of three ion images generated with high mass resolution (± 5 ppm) and high spatial resolution (5 µm). The overlay shows the tissue-specific spatial distributions of a polyphenol glycoside [M+K]+, m/z 603.11107 (green) in the protection sheath coleoptile/coleorhiza covering the main compartments shoot, plumules (first true leaves) and radicle; a phosphatidylcholine [PC(36:4)+K]+, m/z 820.52531 (blue) in the scutellum (monocot cotyledon); and a phosphatidylglycerol [PG(38:2)-H2O+H]+, m/z 785.56910 (red) in the pericarp-seed coat region. MS images were acquired in positive ion mode with 320 x 180 pixels; 5 µm pixel size; and m/z bin width: Δm/z = ± 5 ppm. (c) Overlay of three ion images generated with high mass resolution (± 5ppm) and low spatial resolution (50 µm pixel size) resulting in a loss of spatial information. (d) Overlay of three ion images generated with low mass resolution (Δm/z = 0.1 bin width) and high spatial resolution (5 µm) resulting in a much less distinct resolution, due to neighboring peaks of similar masses which interfere the image generation.
221x116mm (300 x 300 DPI)
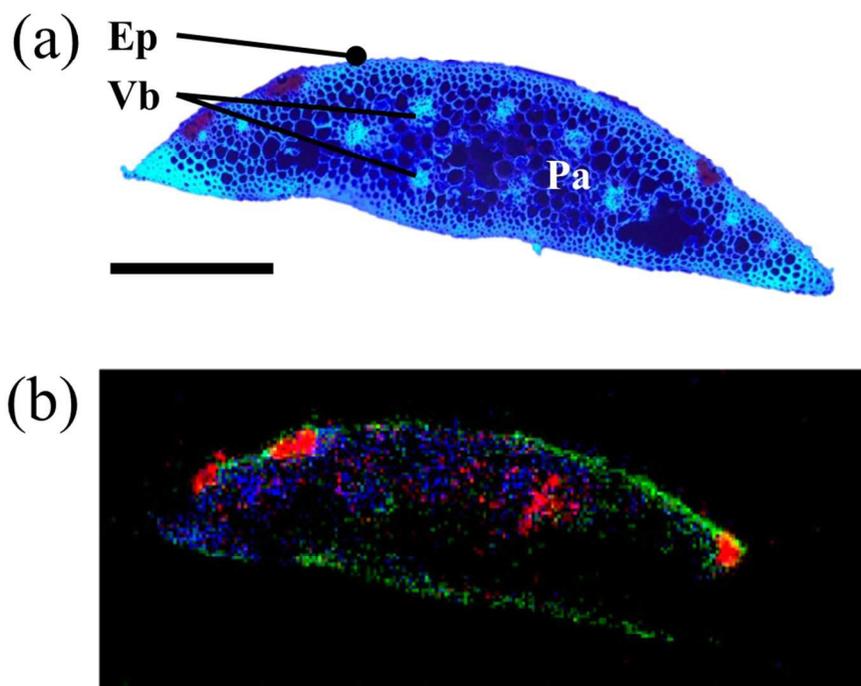
182x93mm (300 x 300 DPI)
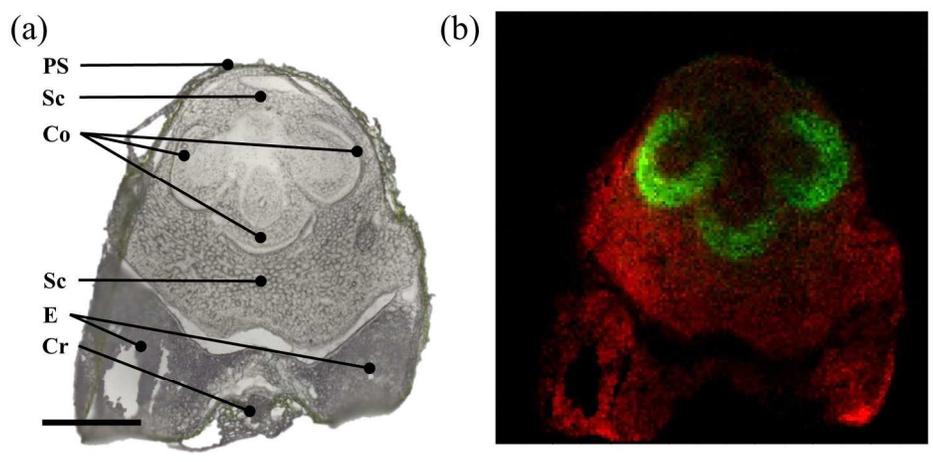
Fig. 5 Mass spectrometry imaging of a wheat rachis section at soft dough stage. (a) Optical image of a 10 μm rachis cross section taken under UV-light. The section was obtained from the center section of inflorescence and shows the epidermis (Ep) and the vascular bundles (Vb) as round inclusions within the central parenchyma cells (Pa). Scale bar 500 μm. (b) Overlay of ion images showing the tissue-specific distributions of a polyphenol glycoside [M+H]+, m/z 565.15518 (green) in the epidermis; a lysophosphatidylcholine [lysoPC(16:0)+K]+, m/z 534.29565 (blue) in the parenchyma; and a pheophytin [pheophytin a+K]+, m/z 909.52908 (red) observed in the parenchyma and epidermis. MS images were generated with 240 x 100 pixels; 10 μm pixel size; m/z bin width: Δm/z = ± 5 ppm.
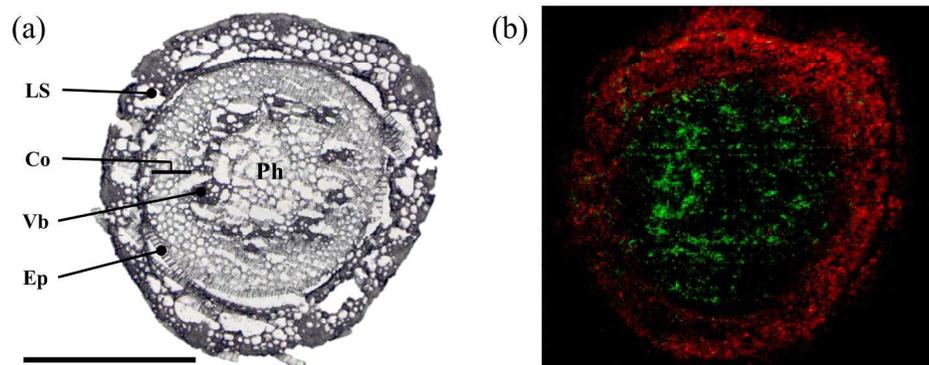99x79mm (300 x 300 DPI)

Fig. 6 MS imaging of a wheat crown at seedling stage. (a) The optical image of a 20 μm crown cross section shows the attached leaf sheath (LS) and the anatomy of seedling stem comprising the epidermis (Ep); the cortex (Co); and the pith (Ph) as central portion including the vascular bundles (Vb). Scale bar 500 μm. (b) Overlay of ion images showing the spatial distributions of a polyphenol glycoside [M+K]+, m/z 565.15518 (red) the leaf sheath; and a phosphatidylcholine [PC(36:4)+K]+, m/z 820.52531 (green) enriched in the vascular tissues and evenly spread within the cortex. MS images were generated with 230 x 210 pixels; 5 μm pixel size; m/z bin width: Δm/z = ± 5 ppm.
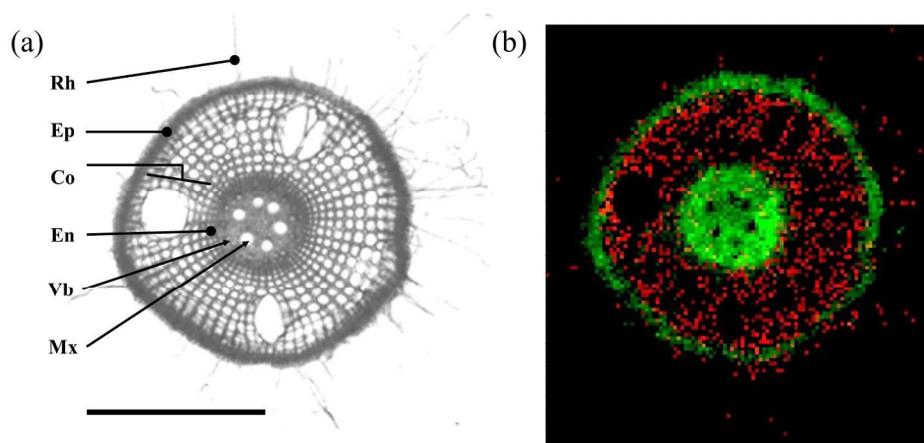201x87mm (300 x 300 DPI)

Fig. 7 Mass spectrometry imaging of a seminal rice root. (a) Optical image of a cross section of a seminal root taken from a region proximal to stem (maturation zone). The image shows the root hairs (Rh) attached to the epidermis (Ep); the central cortex (Co); the endodermis (En) which separates a central root column (stele) containing the vascular bundles (Vb) and the metaxylem vessels (Mx). The holes visible in the cortex are artefacts caused by the drying of root section in the desiccator. Scale bar 500 µm. (b) Overlay of ion images showing the spatial distributions of a [Penta-hexose+K]+, m/z 867.23784 (red) in the cortical layer, and a phosphatidylcholine[PC(36:4)+K]+, m/z 820.52531 (green) in the epidermis and the entire stele, except the metaxylem vessels. MS images were generated with 110 x 120 pixels; 10 µm pixel size; m/z bin width: Δm/z = ± 5ppm.
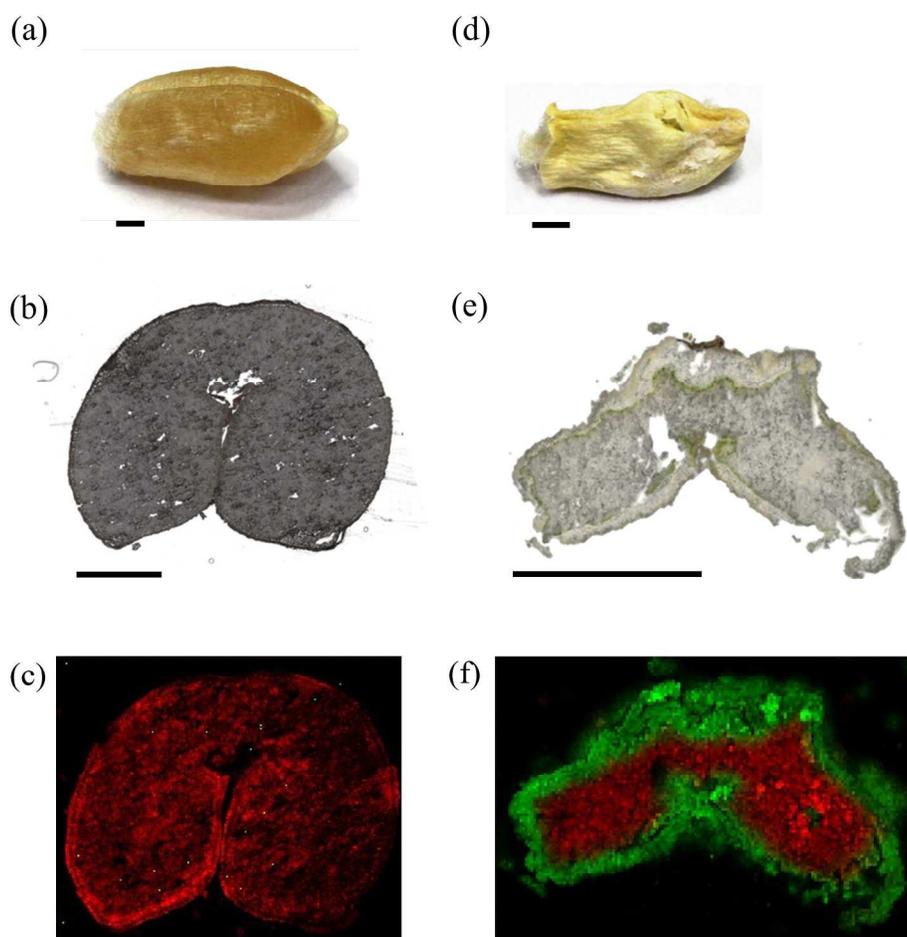208x101mm (300 x 300 DPI)

Fig. 8 Comparative Mass spectrometry imaging of uninfected and F. graminearum-infected wheat seeds at ripening stage. The photographic images show a healthy seed (a) and a seed infected by the fungal pathogen F. graminearum (d) a causal agent of the head blight disease. The seeds were sampled from the highly FHB susceptible spring wheat cv. Florence-Aurore. Scale bars 500 μm. The optical images show 20 μm transverse sections of a healthy (b) and infected seed (e), which were prepared by using the Kuwamoto method. Scale bars 500 μm. Both the photographic (d) and the optical image (e) of the infected seed demonstrate the characteristic weight reduction, shriveled and light-brown appearance associated with a highly susceptible reaction to the FHB disease. The overlay of ion images of healthy (c) and infected seed (f) show the spatial distribution of a [tetra-hexose+K]+ metabolite, m/z 705.18502 (red) in the entire endosperm. In contrast, the metabolite 4-(trimethylammonio)but-2-enoate [M+K]+, m/z 182.05779 (green) located in the entire seed bran and germ was only detected in F. graminearum infected seeds. MS images of healthy seed were generated with 205 x 170 pixels; 20 μm pixel size; m/z bin width: Δm/z = ± 5ppm. MS images of infected seed were generated with 155 x 105 pixels; 15 μm pixel size; m/z bin width: Δm/z = ± 5 ppm.
187x185mm (300 x 300 DPI)

(b)

(e)

Leaf blade (wheat, 10 μm)

(f)

Rachis (wheat, 10 μm)

Seed (oilseed rape, 10 μm)

(c)

(g)

Root, proximal (rice, 10 μm)

Stem (oilseed rape, 20 μm)

(d)

(h)

(a)

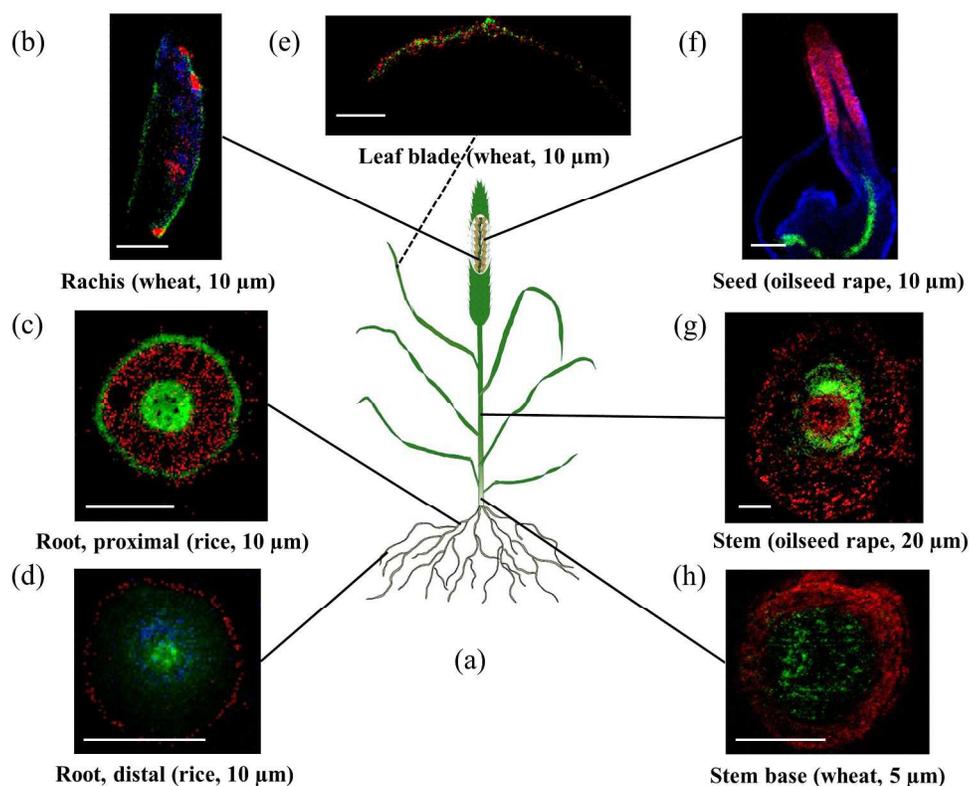**Root, distal (rice, 10 μm)**

Stem base (wheat, 5 μm)

Fig. 9 Overview on the different plant structures which have been made available to high- resolution MS imaging. Scale bars in all images 500 μm. (a) Sketch of a plant. (b) MS image of wheat inflorescence rachis measured at 10 μm pixel size, details are given in Fig. 5. (c) MS image of a seminal proximal rice root (maturation zone) measured at 10 μm pixel size; details are given in Fig. 7. (d) MS image of a seminal distal rice root (elongation zone) measured at 10 μm pixel size, details are given in Supporting information, Fig S9. (e) MS image of a wheat leaf blade measured at 10 μm pixel size, details are given in Supporting information, Fig. S12. (f) MS image of germinating oilseed rape at 10 μm pixel size, details are given in Fig. 1. (g) MS image of oilseed rape stem at 20 μm pixel size, details are given in Supporting information, Fig. S13. (h) MS image of wheat stem base at 5 μm pixel size, detail are given in Fig. 6.
217x178mm (300 x 300 DPI)